Quantized Conductance in Topological Insulators Revealed by the Shockley-Ramo Theorem

Paul Seifert,[1,2] Marinus Kundinger,[1,2] Gang Shi,[3] Xiaoyue He,[3] Kehui Wu,[3] Yongqing Li,[3] Alexander Holleitner,[1,2,*] and Christoph Kastl[1,2,4]

[1]*Walter Schottky Institut and Physics Department, Technical University of Munich, Am Coulombwall 4a, 85748 Garching, Germany*

[2]*Munich Center for Quantum Science and Technology (MCQST), Schellingstrasse 4, D-80799 München, Germany*

[3]*Institute of Physics, Chinese Academy of Sciences, Beijing 100190, China*

[4]*Molecular Foundry, Lawrence Berkeley National Laboratory, 1 Cyclotron Road, Berkeley, California 94720, USA*

(Received 4 September 2018; revised manuscript received 14 February 2019; published 12 April 2019)

Crystals with symmetry-protected topological order, such as topological insulators, promise coherent spin and charge transport phenomena even in the presence of disorder at room temperature. We demonstrate how to image and read out the local conductance of helical surface modes in the prototypical topological insulators Bi_2Se_3 and $BiSbTe_3$. We apply the so-called Shockley-Ramo theorem to design an optoelectronic probe circuit for the gapless surface states, and we find a well-defined conductance quantization at $1e^2/h$ within the experimental error without any external magnetic field. The unprecedented response is a clear signature of local spin-polarized transport, and it can be switched on and off via an electrostatic field effect. The macroscopic, global readout scheme is based on an electrostatic coupling from the local excitation spot to the readout electrodes, and it does not require coherent transport between electrodes, in contrast to the conventional Landauer-Büttiker description. It provides a generalizable platform for studying further nontrivial gapless systems such as Weyl semimetals and quantum spin-Hall insulators.

DOI: 10.1103/PhysRevLett.122.146804

In radiation detectors, electronic signal formation relies on the so-called Shockley-Ramo (SR) theorem [1,2], which is distinct to the Landauer-Büttiker formalism describing mesoscopic transport between electrodes [3,4]. Instead, radiation entering the detector locally creates free charge carriers in an insulating medium. These local charges never reach an electrode, but a macroscopic current is electrostatically induced between the electrodes independent of the excitation position within the detector volume [1,2]. However, only those local current components contribute which align parallel to the so-called weighting field describing the electrostatic potential for a specific geometry and electrode configuration.

The same framework can describe the detection of local currents, such as local photoexcitations, in conductive media [5]. By solving the continuity equation for the locally excited current density $\boldsymbol{j}_{\mathrm{loc}}(x,y)$ and the globally measured detector current I at the contacts, one can show that $\boldsymbol{j}_{\mathrm{loc}}(x,y)$ induces a macroscopic signal

$$I = A \int \boldsymbol{j}_{\mathrm{loc}}(x,y) \cdot \nabla\phi(x,y)dxdy, \tag{1}$$

although the locally excited charges are never collected at the electrodes [5]. Hereby, $\nabla\phi(x,y)$ is an auxiliary weighting field derived from a suitable potential $\phi(x,y)$ within the device, and A considers the resistance of the overall circuitry. The weighting field coincides with the electrostatic field in the absence of a transversal Hall conductivity [5]. For two-dimensional systems, this becomes especially useful because all fields are in plane and accessible to external probes, such as a focused laser excitation. In turn, the SR theorem explains, e.g., nonlocal photoresponses in graphene at floating electrodes, which are not directly connected to the readout electrodes [6]. While the SR response is trivial for material anisotropies as a source of the local photocurrent, such as potential fluctuations [7] or p-n junctions [8], we reveal that it also allows detecting currents which are more intrinsic in nature. In particular, we determine the local conductance of topological surface states using a local photoexcitation and a global electronic readout.

Topological insulators exhibit a gapped dispersion in the bulk and symmetry protected, gapless surface states described by helical Dirac fermions [9–12]. The spin degeneracy is lifted at the surface since states with opposite helicity reside on opposite surfaces. Applying an optoelectronic SR detection scheme to field effect devices made of Bi_2Se_3 and $BiSbTe_3$ topological insulator films, we uncover a well-defined conductance localized at the edges of the films. Intriguingly, the average value of the detected conductance coincides with the conductance quantum of

$1e^2/h$ within the experimental error, suggesting that the transport occurs via a single, nondegenerate surface mode. We show that the field effect from the back electrode modulates the weighting field such that, for a photoexcitation at the films' edges, the local conductance is dominated by a broken symmetry of propagating modes in the direction perpendicular to the edges. We argue that the current due to surface modes propagating toward the sample edge is effectively cut off by scattering at the edges, which in turn yields a net current of surface modes propagating away from the sample edges. This symmetry breaking is otherwise not detectable because a conventional transport measurement, and also the local SR measurement without the gate field, detects only currents parallel to the edge. This complements conventional transport experiments which achieve the differentiation between surface and bulk in topological insulators either by suppressing bulk conduction via electrostatic doping and growth of materials with a reduced bulk conductivity [13–15] or by selectively addressing the helical surface states via optoelectronic methods [16–18].

Figure 1(a) sketches our SR scheme based on an in-plane symmetry breaking in prototypical Bi_2Se_3 circuits on a $SrTiO_3$ substrate [14,15]. The Bi_2Se_3 film is contacted by source and drain electrodes on the left and right, but the weighting field $\nabla\phi$ is dominated by a gate potential $V_{\mathrm{gate}} > 0$, applied at the back of the substrate. Then, $\nabla\phi$ aligns perpendicular to the edge of the film, breaking the in-plane symmetry of an otherwise isotropic local current $\boldsymbol{j}_{\mathrm{loc}}(x, y)$. When charges are locally added to the system, e.g., by optical excitation [red cone in Fig. 1(a)], a net current into the sample is detected (white arrow). There are simply no states flowing out of the Bi_2Se_3 film. Assuming this symmetry breaking and the Fermi energy to be within the surface states, one expects to measure the properties of surface states propagating into the sample. Such reasoning implies that the propagation of surface states toward the sample edge is cut off compared to the propagation of surface states away from the sample edge, possibly by spin-scattering sources localized at the edge. Since the materials are gapless, added charges always end up at the Fermi energy, which also holds for interband photoexcitation after thermalization and relaxation of hot charge carriers. Importantly, the symmetry breaking is not achieved for ungated devices [Fig. 1(b)]. There, $\nabla\phi$ extends from source to drain within the Bi_2Se_3 film, and we detect only charges moving parallel to the edge. The corresponding global response is zero because locally two states contribute with opposite directions (the two white arrows).

The anisotropic fields in Fig. 1(a) are realized with a gate electrode at the back side of the substrate. Since the films' lateral footprint is much smaller than the extension of the gate [Fig. 1(c)], this device resembles a plate-wire configuration with an anisotropic field distribution $\boldsymbol{E}_{\mathrm{sub}}$. The large change in dielectric constant at the vacuum/$SrTiO_3$ interface aligns the field parallel to the interface near the film edges, which enhances the in-plane field E_x [the arrows in Fig. 1(d)]. The simulated peak field is $\sim 10^7$ V m^{-1} at $V_{\mathrm{gate}} = 100$ V when assuming $\varepsilon_{\mathrm{SrTiO3}} = 10^4$ at 5 K [19]. Figure 1(e) shows the out-of-plane field E_z extending below the Bi_2Se_3 film, as expected. Figure 1(f) depicts the overall device circuitry. We locally excite the Bi_2Se_3 film using a focused laser ($E_{\mathrm{photon}} = 1.5$ eV, red cone). Two electrodes act as low-impedance contacts for the macroscopic current signal I, and they provide the gate's reference potential. A high-impedance amplifier is wired to a third contact, for simultaneous measurement of the voltage V. Then, scanning the laser across the device, this three-terminal circuitry defines a local conductance $G(x, y) = I(x, y)/V(x, y)$ for the photogenerated carriers for each position (x, y). For details, see the Supplemental Material [20].

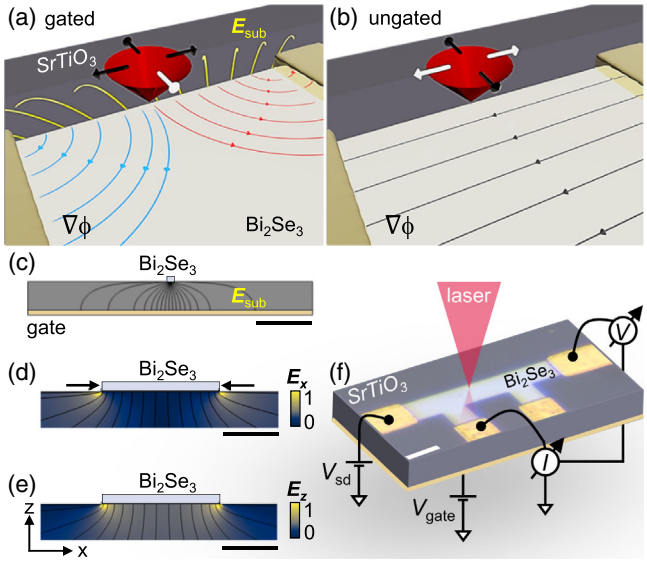

FIG. 1. Gated and ungated Bi_2Se_3 films on $SrTiO_3$ substrates. (a) A gate voltage V_{gate} at the back side of the substrate aligns the weighting field $\nabla\phi$ perpendicular to the film's edge. A local excitation (red cone) generates a net current perpendicular to the edge (white arrow) coupling to the source-drain electrodes (left and right) through $\nabla\phi$. (b) Without the gate, only currents parallel to the edge (white arrows) couple to the electrodes. (c) Simulated electric field between gate and Bi_2Se_3 film (side view). Scale bar, 1 mm. (d),(e) Magnified view of the anisotropic electric field $\boldsymbol{E}_{\mathrm{sub}}$. The in-plane ($E_x$) and out-of-plane ($E_z$) fields are in units of 10^7 V m^{-1} ($V_{\mathrm{gate}} = 100$ V). Black lines indicate the electric field. Scale bars, 5 μm. (f) Three-terminal configuration for optoelectronic measurements. Scale bar, 5 μm.

Figures 2(a) and 2(b) show current $I(x, y)$ and voltage maps $V(x, y)$ of an n-type Bi_2Se_3 device for $V_{\mathrm{gate}} > 0$ V. All measurements were at zero source-drain bias, $T = 4.2$ K, and $E_{\mathrm{photon}} = 1.5$ eV. The current is measured between the contacts labeled S and D [Fig. 2(a)], while the voltage is concurrently measured between $V+$ and $V-$ [Fig. 2(b)].

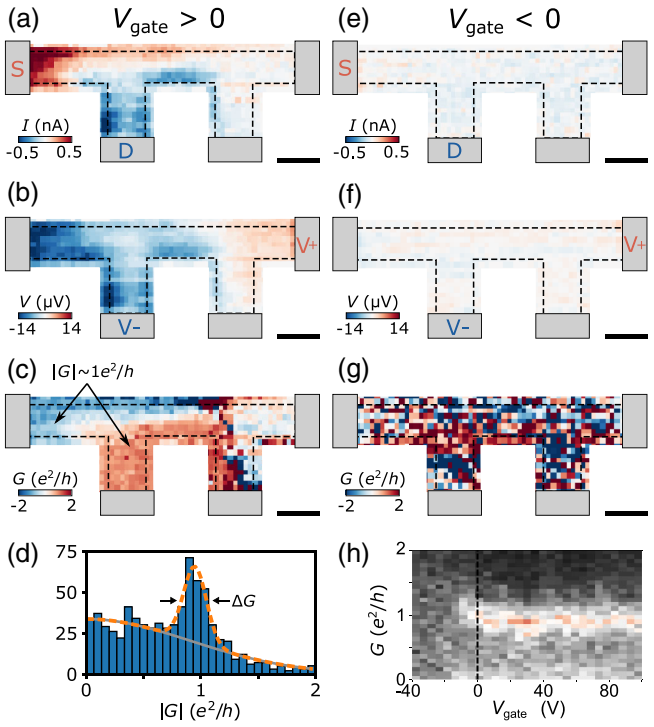

FIG. 2. Quantized conductance in Bi_2Se_3 circuits. (a)–(c) Spatial maps of the current I, the voltage V, and the local conductance $G = I/V$ at positive gate voltage ($V_{gate} = 15$ V). The laser-induced current (voltage) is measured between S and D ($V+$ and $V-$). (d) The histogram across all positions shows a defined conductance (orange dashed line) with mean $|G| = 0.94e^2/h$, full width at half maximum $\Delta G = 0.24e^2/h$, and a broad background signal (gray line). (e)–(g) For negative and zero gating, the quantized conductance detection is switched off ($V_{gate} = -30$ V), and the response is dominated by potential fluctuations. Dashed lines indicate the edge of the circuit. Scale bars, 5 μm. (h) For all values of $V_{gate} > 0$, a well-defined conductance is observed close to e^2/h.

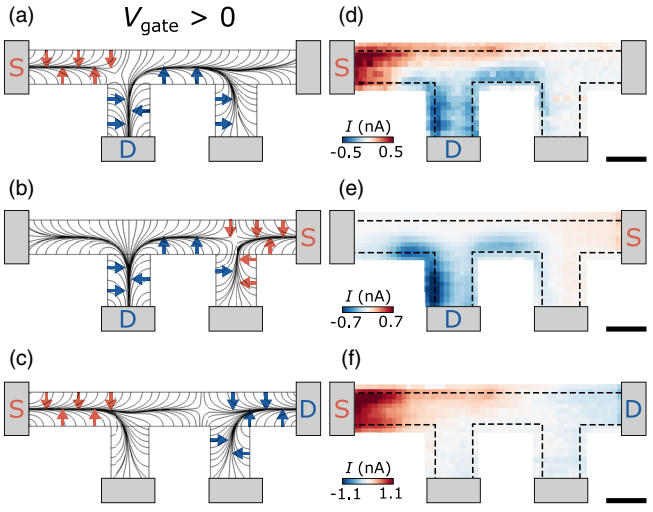

FIG. 3. Different circuit configurations. (a)–(c) Simulated field distribution and (d)–(f) measured current between source (S) and drain (D). The other contacts are floating. Arrows indicate the local current $\boldsymbol{j}_{loc}(x, y)$. The sign of the global signal is determined by the coupling of $\boldsymbol{j}_{loc}(x, y)$ into S and D through the weighting field. Red (blue) arrows indicate a global current into S (D). The dashed lines indicate the edge of the circuit. Scale bars, 5 μm.

Within our spatial resolution (~1–2 μm), we detect a distinct conductance $G(x, y)$ [Fig. 2(c)] at the edges of the device (the dashed lines). The histogram of all $G(x, y)$ exhibits a well-defined conductance with mean $|G| = 0.94e^2/h$ and full width at half maximum $\Delta G = 0.24e^2/h$ [the dashed orange distribution in Fig. 2(d)] on top of a broader background. The peak near $1e^2/h$ implies that the local transport is carried by a spin-polarized mode of the topological surface state. Figures 2(e)–2(h) present corresponding data for $V_{gate} < 0$ V (see also Ref. [20]). We observe that the edge response is suppressed for this gate setting. Then, a photothermoelectric current dominates, driven by local fluctuations of the Seebeck coefficient in the surface states [7]. Here, this effect can be slightly resolved within the noise level [Figs. 2(e)–2(g)], and $G(x, y)$ appears to be random [Fig. 2(g)], which explains the background distribution in Fig. 2(d). The sign of $G(x, y)$ is determined by the local current direction. The detection of the quantized conductance is switched on as the gate voltage is increased to $V_{gate} > 0$ [Fig. 2(h)].

According to the SR theorem, different configurations of floating and grounded electrodes change the weighting field and, consequently, the macroscopic response [1,2,5]. Figure 3 depicts simulated weighting fields [the black lines in Figs. 3(a)–3(c)] and measured current maps [Figs. 3(d)–3(f)] for different configurations. In all cases, source (S) and drain (D) are grounded, and no bias is applied. All other contacts are floating. We apply boundary conditions such that the fields terminate perpendicularly at the sample edges and contacts [5]. The red and blue arrows in Fig. 3(a) indicate locally excited currents $\boldsymbol{j}_{loc}(x, y)$ perpendicular to the boundaries resulting from the in-plane symmetry breaking. These currents couple via the weighting field either to source (red arrows) or to drain (blue arrows). With Eq. (1), this determines the sign of the global current. The simulations and experiments are consistent with the expected SR response. In Figs. 3(d) and 3(e), we can accurately explain the nonlocal negative current (blue) between D and the floating contact next to it. It also explains how currents $\boldsymbol{j}_{loc}(x, y)$ with opposite polarity (indicated by direction of arrows) at opposite edges yield the same polarity of the global current $I(x, y)$. Experimentally, there is an asymmetry in the contacts with respect to the magnitude of the current [cf. S and D in Fig. 3(f)] likely caused by the varying contact resistances for different electrodes [20]. To reproduce the observed asymmetry, we implemented asymmetric boundary conditions at the contacts for the simulations [20].

As-grown Bi_2Se_3 films are typically n doped due to defects, and the Fermi level is situated above the gap

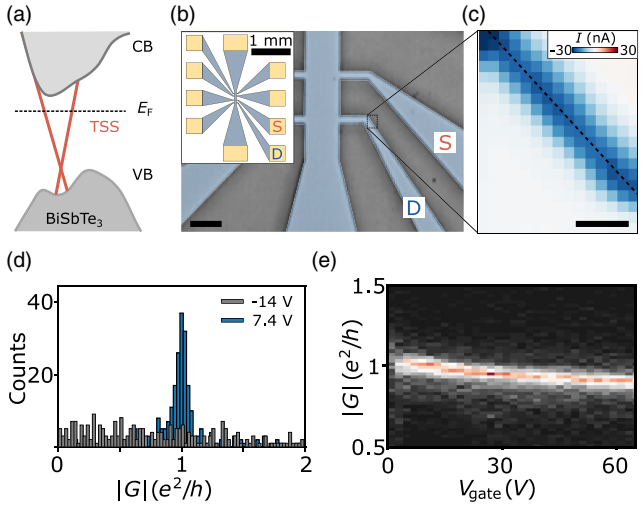

FIG. 4. Enhanced quantization in $BiSbTe_3$. (a) Schematic band structure of $BiSbTe_3$ with conduction band (CB), valence band (VB), topological surface state (TSS), and Fermi level E_F. (b) $BiSbTe_3$ Hall bar with source (S) and drain (D). Scale bar, 50 μm. (c) $I(x,y)$ of the area indicated by the rectangle in (b) ($V_{\mathrm{gate}} = 7.4$ V). The current is localized at the edge (dashed line). Scale bar, 1 μm. (d) Conductance histogram for the measurement in (c) with $|G| = 1.003e^2/h$ and $\Delta G = 0.1e^2/h$ (blue bars). At $V_{\mathrm{gate}} = -14$ V, the quantized conductance detection is switched off (gray bars). (e) $|G|$ as a function of V_{gate}.

for positive V_{gate} [15,21]. Then, warping of the surface dispersion and the coexistence of surface with bulk states open additional scattering channels [22–24]. Thereby, we explain the reduced mean $|G| < 1e^2/h$, the broad ΔG, and the background in Fig. 2(d). Therefore, we studied $BiSbTe_3$ films, where the Fermi level is in the gap for $V_{\mathrm{gate}} = 0$ V, albeit not necessarily at the Dirac point [Fig. 4(a)] [25]. The films are fabricated into macroscopic Hall bars [Fig. 4(b)]. Again, the photocurrent is clearly localized at the edges [see Fig. 4(c) and the Supplemental Material [20]]. The histogram of $|G|$ shows a sharp quantization with $|G| = 1.003e^2/h$ and $\Delta G = 0.1e^2/h$ [Fig. 4(d)]. The quantized conductance appears at $V_{\mathrm{gate}} > 0$ V at $|G| = 1e^2/h$ [Fig. 4(e)], and it decreases to $|G| \approx 0.9e^2/h$ for more positive voltages, which we interpret to be a signature of increased scattering or hybridization between bulk and surface states. For $V_{\mathrm{gate}} > 50$ V, the gate capacitance decreases explaining the saturation of $|G|$. These millimeter-sized circuits exceed by far the relevant transport length scales demonstrating that the quantized conductance must be understood as a local effect and that the detection is consistent with a long-range SR response. While the smaller circuits (Figs. 2 and 3) allowed us to image the full optoelectronic response for different contact geometries, these larger circuits show sharper quantization, which we tentatively attribute to the decreasing contribution of "conventional" photocurrents with increasing circuit size. In the common transport formalism, a quantized conductance ne^2/h results from ballistic transmission of n nondegenerate modes between reservoirs of a continuum of 2D modes, i.e., the contacts. In this mesoscopic Landauer-Büttiker formalism, one measures $I(x,y)$ via two contacts and probes the voltage $V(x,y)$ with the two remaining contacts [26]. For all such standard wirings, we could not concurrently detect a finite I and V to determine a well-defined $G(x,y)$ [20]. Therefore, in our understanding, we cannot apply the Landauer-Büttiker formalism. Instead, Fig. 3(c) explains why we cannot measure a signal in a four-terminal wiring: there is no position (x,y) in the circuit connecting to all four probes (the same applies to all further wirings).

By contrast, our experiments suggest that within the SR scheme, a coherent charge and spin transport between the excitation spot and the contact is not a prerequisite for detecting a quantized conductance. The lateral footprint of our circuits exceeds by far the surface states' coherence length (~100 nm) [27]. Yet, it is crucial to utilize a focused laser spot. We do not detect a conductance signal for a defocused excitation of the circuits.

The mechanism generating the photocurrent (~nA) at the sample edge is apparently about 2 orders of magnitude more efficient than the photothermoelectric effect (~pA) [7]. The latter appears as a seemingly random current due to potential fluctuations away from the edges [cf. Figs. 1(e)–1(g)]. We further exclude a photogalvanic effect and spin-Hall photoconductance since the signal is independent of laser polarization (see Refs. [16,17,28] and the Supplemental Material [20]). The quantized conductance is observable up to $T \sim 10$ K, and in this range, G is independent of temperature [20] suggesting that the microscopic mechanism is also different from the predicted "squeezed edge currents" in multivalley insulators [29]. Rather, our findings are consistent with a local current perpendicular to the sample edge (Figs. 1 and 3). Here, a net photocurrent is generated if the propagation of surface states toward the sample edge is effectively cut off compared to the propagation of surface states away from the edge, possibly by spin-scattering sources localized at the edge. Then, in our understanding, the weighting field acts as a directional momentum filter perpendicular to the edges independent of the photoexcitation and relaxation processes of the hot charge carriers [30]. The optical excitation at 1.5 eV involves interband transitions between both surface and bulk states [31]. In our understanding, the observed transport at e^2/h occurs at the Fermi level within the laser spot because initial thermalization and relaxation occur on a subpicosecond timescale [32]. Different length scales govern the local response, which are the Thomas-Fermi screening length (a few nanometers), the inelastic mean free path (~10–100 nm), the diffusion length of hot charge carriers (several hundred nanometers), and the laser spot (1 to 2 μm). The excited state population locally increases the chemical potential according to the compressibility of the surface states, and it can persist up to hundreds of picoseconds [33,34]. For the $BiSbTe_3$ films, the Fermi level

is within the gap such that the conductance of the surface states dominates. This transport is then detected macroscopically through $\nabla\phi(x, y)$ at the source and drain contacts (Fig. 1). Ultimately, we expect the smallest relevant length scale to be the screening of the hard-wall potential at the edges.

Our SR model explains the switching of the photoresponse, which is at first sight counterintuitive due to the gapless surface state. Furthermore, we accurately predict polarity, long-range character, and apparent nonlocality of the conductance. In all of our experiments, the quantized conductance is resolved only at $V_{\mathrm{gate}} > 0$, independent of the material. Yet, the simple electrostatic model [Figs. 3(a)–3(c)] would simply reverse the field for $V_{\mathrm{gate}} < 0$. However, this does, e.g., not consider defects at the etched boundaries of the circuits. As known from semiconducting surfaces, such defects can give rise to an interfacial Fermi-level pinning. A corresponding Fermi-level pinning at the circuit boundaries with an overall negative charge accumulation would support the electrostatics for $V_{\mathrm{gate}} > 0$. For $V_{\mathrm{gate}} < 0$, such a Fermi-level pinning would partially compensate for the gating at the boundaries and would move the field lines toward the interior of the circuits. Then, the photocurrent would be similar to the pristine 2D situation for $V_{\mathrm{gate}} < 0$, as is consistent with the measurements. To gain further insight into the microscopic origins, it will be necessary to disentangle the effects of field enhancement, Thomas-Fermi screening, potential fluctuations, and gating of bottom vs top surface. Additional top gates made from graphene with an *h*-BN spacer may help to differentiate between bottom and top surfaces and to tune into a quantized conductance regime also for $V_{\mathrm{gate}} < 0$. Near field measurements may allow for exploring the optoelectronic processes at the relevant length scales [35]. Currently, the "lateral resolution" is limited to ~300 nm [20].

Overall, we demonstrate a novel optoelectronic detection scheme that applies the SR theorem to conductors, which allows us to locally excite, yet macroscopically read out, the quantized conductance of topological surface states. This readout scheme can provide a generalizable platform for studying local transport in further nontrivial gapless systems such as graphene, Weyl semimetals, or quantum spin-Hall insulators [35–37].

During the revision process, we became aware of related work [38] where an analogous photoresponse near the edges of graphene circuits was observed. The findings were similarly explained by our proposed mechanism of an asymmetric scattering of photoexcited carriers at the circuit edges in combination with a distorted weighting field at lithographically defined constrictions in the planar graphene circuits.

We thank J. Song for the in-depth discussions. This work was supported by the DFG via SPP 1666 (Grant No. HO 3324/8) and the Munich Center for Quantum Science and Technology (MCQST)—EXC-2111–390814868, the Center of NanoScience (CeNS) in Munich, and the Munich Quantum Center (MQC). C.-K. acknowledges funding by the Molecular Foundry supported by the Office of Science, Office of Basic Energy Sciences, of the U.S. Department of Energy under Contract No. DE-AC02-05CH11231. Y. L. thanks the support from NSFC (Grant No. 61425015) and CAS (Grant No. XDB28000000).

*holleitner@wsi.tum.de

[1] S. Ramo, Proc. IRE **27**, 584 (1939).
[2] W. Shockley, J. Appl. Phys. **9**, 635 (1938).
[3] C. W. J. Beenakker and H. van Houten, in *Solid State Physics*, edited by H. Ehrenreich and D. Turnbull (Academic Press, New York, 1991), pp. 1–228.
[4] Y. Imry and R. Landauer, Rev. Mod. Phys. **71**, S306 (1999).
[5] J. C. W. Song and L. S. Levitov, Phys. Rev. B **90**, 075415 (2014).
[6] J. Park, Y. H. Ahn, and C. Ruiz-Vargas, Nano Lett. **9**, 1742 (2009).
[7] C. Kastl, P. Seifert, X. He, K. Wu, Y. Li, and A. Holleitner, 2D Mater. **2**, 024012 (2015).
[8] A. L. Yeats, Y. Pan, A. Richardella, P. J. Mintun, N. Samarth, and D. D. Awschalom, Sci. Adv. **1**, e1500640 (2015).
[9] L. Fu and C. L. Kane, Phys. Rev. B **76**, 045302 (2007).
[10] Y. L. Chen, J. G. Analytis, J.-H. Chu, Z. K. Liu, S.-K. Mo, X. L. Qi, H. J. Zhang, D. H. Lu, X. Dai, Z. Fang, S. C. Zhang, I. R. Fisher, Z. Hussain, and Z.-X. Shen, Science **325**, 178 (2009).
[11] H. Zhang, C.-X. Liu, X.-L. Qi, X. Dai, Z. Fang, and S.-C. Zhang, Nat. Phys. **5**, 438 (2009).
[12] M. König, S. Wiedmann, C. Brüne, A. Roth, H. Buhmann, L. W. Molenkamp, X.-L. Qi, and S.-C. Zhang, Science **318**, 766 (2007).
[13] X. He, T. Guan, X. Wang, B. Feng, P. Cheng, L. Chen, Y. Li, and K. Wu, Appl. Phys. Lett. **101**, 123111 (2012).
[14] J. Chen, H. J. Qin, F. Yang, J. Liu, T. Guan, F. M. Qu, G. H. Zhang, J. R. Shi, X. C. Xie, C. L. Yang, K. H. Wu, Y. Q. Li, and L. Lu, Phys. Rev. Lett. **105**, 176602 (2010).
[15] G. Zhang, H. Qin, J. Chen, X. He, L. Lu, Y. Li, and K. Wu, Adv. Funct. Mater. **21**, 2351 (2011).
[16] J. W. McIver, D. Hsieh, H. Steinberg, P. Jarillo-Herrero, and N. Gedik, Nat. Nanotechnol. **7**, 96 (2012).
[17] P. Seifert, K. Vaklinova, S. Ganichev, K. Kern, M. Burghard, and A. W. Holleitner, Nat. Commun. **9**, 331 (2018).
[18] C. Kastl, C. Karnetzky, H. Karl, and A. W. Holleitner, Nat. Commun. **6**, 6617 (2015).
[19] K. A. Müller and H. Burkard, Phys. Rev. B **19**, 3593 (1979).
[20] See Supplemental Material at http://link.aps.org/supplemental/10.1103/PhysRevLett.122.146804 for material growth, experimental and numerical methods, and additional data.
[21] J. Chen, X. Y. He, K. H. Wu, Z. Q. Ji, L. Lu, J. R. Shi, J. H. Smet, and Y. Q. Li, Phys. Rev. B **83**, 241304(R) (2011).
[22] L. Fu, Phys. Rev. Lett. **103**, 266801 (2009).

[23] P. Rüßmann, P. Mavropoulos, and S. Blügel, J. Phys. Chem. Solids, DOI: 10.1016/j.jpcs.2017.12.009 (2004).
[24] S. Kim, M. Ye, K. Kuroda, Y. Yamada, E. E. Krasovskii, E. V. Chulkov, K. Miyamoto, M. Nakatake, T. Okuda, Y. Ueda, K. Shimada, H. Namatame, M. Taniguchi, and A. Kimura, Phys. Rev. Lett. **107**, 056803 (2011).
[25] J. Kellner, M. Eschbach, J. Kampmeier, M. Lanius, E. Młyńczak, G. Mussler, B. Holländer, L. Plucinski, M. Liebmann, D. Grützmacher, C. M. Schneider, and M. Morgenstern, Appl. Phys. Lett. **107**, 251603 (2015).
[26] Y. Xu, I. Miotkowski, C. Liu, J. Tian, H. Nam, N. Alidoust, J. Hu, C.-K. Shih, M. Z. Hasan, and Y. P. Chen, Nat. Phys. **10**, 956 (2014).
[27] H. Steinberg, J.-B. Laloë, V. Fatemi, J. S. Moodera, and P. Jarillo-Herrero, Phys. Rev. B **84**, 233101 (2011).
[28] H. Plank, J. Pernul, S. Gebert, S. N. Danilov, J. König-Otto, S. Winnerl, M. Lanius, J. Kampmeier, G. Mussler, I. Aguilera, D. Grützmacher, and S. D. Ganichev, Phys. Rev. Mater. **2**, 024202 (2018).
[29] J. C. W. Song and G. Vignale, arXiv:1805.05955.
[30] I. Kyriakou, J. H. Jefferson, G. Giavaras, M. Fearn, and C. J. Lambert, Phys. Rev. B **76**, 045316 (2007).
[31] Y. Pan, Q.-Z. Wang, A. L. Yeats, T. Pillsbury, T. C. Flanagan, A. Richardella, H. Zhang, D. D. Awschalom, C.-X. Liu, and N. Samarth, Nat. Commun. **8**, 1037 (2017).
[32] A. Crepaldi, B. Ressel, F. Cilento, M. Zacchigna, C. Grazioli, H. Berger, P. Bugnon, K. Kern, M. Grioni, and F. Parmigiani, Phys. Rev. B **86**, 205133 (2012).
[33] D. S. L. Abergel and S. Das Sarma, Phys. Rev. B **87**, 041407 (R) (2013).
[34] P. Seifert, K. Vaklinova, K. Kern, M. Burghard, and A. Holleitner, Nano Lett. **17**, 973 (2017).
[35] A. Woessner, P. Alonso-González, M. B. Lundeberg, Y. Gao, J. E. Barrios-Vargas, G. Navickaite, Q. Ma, D. Janner, K. Watanabe, A. W. Cummings, T. Taniguchi, V. Pruneri, S. Roche, P. Jarillo-Herrero, J. Hone, R. Hillenbrand, and F. H. L. Koppens, Nat. Commun. **7**, 10783 (2016).
[36] S. Tang *et al.*, Nat. Phys. **13**, 683 (2017).
[37] S. Wu, V. Fatemi, Q. D. Gibson, K. Watanabe, T. Taniguchi, R. J. Cava, and P. Jarillo-Herrero, Science **359**, 76 (2018).
[38] Q. Ma, C. H. Lui, J. C. W. Song, Y. Lin, J. F. Kong, Y. Cao, T. H. Din, N. L. Nair, W. Fang, K. Watanabe, T. Taniguchi, S.-Y. Xu, J. Kong, T. Palacios, N. Gedik, N. M. Gabor, and P. Jarillo-Herrero, Nat. Nanotechnol. **14**, 145 (2019).